Lowering Internal Friction of 0D–1D–2D Ternary Nanocomposite-Based Strain Sensor by Fullerene to Boost the Sensing Performance

Xinlei Shi, Shuiren Liu, Yang Sun, Jiajie Liang,* and Yongsheng Chen

The development of strain sensors with both large strain range (>50%) and high gauge factor (>100) is a grand challenge. High sensitivity requires material to perform considerable structural deformation under tiny strain, whereas high stretchability demands structural connection or morphological integrity for materials upon large deformation, yet both features are hard to be achieved in one thin film. A new 0D–1D–2D ternary nanocomposite–based strain sensor is developed that possesses high sensitivity in broad working strain range (gauge factor 2392.9 at 62%), low hysteresis, good linearity, and long-term durability. The skin-mountable strain sensor, fabricated through one-step screen-printing process, is made of 1D silver nanowire offering high electrical conductivity, 2D graphene oxide offering brittle layered structure, and 0D fullerene offering lubricity. The fullerene constitutes a critical component that lowers the friction between graphene oxide–based layers and facilitates the sliding between adjacent layers without hurting the brittle nature of the nanocomposite film. When stretching, layer slippage induced by fullerene can accommodate partial applied stress and boost the strain, while cracks originating and propagating in the brittle nanocomposite film ensure large resistance change over the whole working strain range. Such high comprehensive performance renders the strain sensor applicable to full-spectrum human motion detection.

1. Introduction

In recent years, a great deal of progress has been achieved in the development of skin-mountable and wearable electronics for the realization of next-generation electronic applications.[1–3] In particular, resistive-type stretchable strain sensors, which

X. Shi, S. Liu, Y. Sun, Prof. J. Liang, Prof. Y. Chen
School of Materials Science and Engineering
National Institute for Advanced Materials
Nankai University
Tianjin 300350, P. R. China
E-mail: liang0909@nankai.edu.cn
Prof. J. Liang, Prof. Y. Chen
Key Laboratory of Functional Polymer Materials of Ministry of Education
College of Chemistry
Nankai University
Tianjin 300350, P. R. China
Prof. J. Liang
Tianjin Key Laboratory of Metal and Molecule-Based Material Chemistry
and Collaborative Innovation Center of Chemical Science and
Engineering (Tianjin)
Nankai University
Tianjin 300350, P. R. China

transduce mechanical deformation into the change of electrical resistance when stretching, are considered as indispensable component in several emerging application fields including human motion detection, human healthy monitoring, soft robotics, and so on.[3–6] The sensing performance of such strain sensors is normally evaluated by a range of comprehensive requirements including high sensitivity (gauge factor (GF)), large stretchability (working strain range), good linearity, long-term durability, and reliability, low hysteresis, fabrication simplicity, etc. Among these factors, GF, which refers to the slope of the curve of relative resistance change versus applied strain (defined by $((R - R_0)/R_0)/\varepsilon$, where $(R - R_0)/R_0$ refers to relative resistance change and ε refers to tensile strain), stretchability, which refers to the reversible working strain, and linearity, which makes the sensing and calibration process simple and reliable, are the most crucial and investigated.[6] These demands become even more desperately for practical applications on full-spectrum human motion, health and activity-related detection or monitoring, where working strain range broader than 50% and gauge factor higher than 100 (in full working strain range) are required simultaneously for accurate detection of subtle and large strains.[6,7] However, there is a trade-off relationship between the features of "high sensitivity" and "high linearity and stretchability" due to their conflict structural requirements on the sensing materials, which severely limits the development of stretchable strain sensor.[6,8–10]

Cracks generating and propagating in rigid or brittle conductive thin film/network during stretching and thus greatly limiting the electrical conduction through the thin film/network is the main mechanism exploited to design strain sensors with high sensitivity.[11] A variety of strain sensors based on rigid or brittle metal nanowires network,[7,12] metal nanoparticle thin film,[13] graphene or graphite thin film,[9,14–17] and metal thin films,[11,18] with good response linearity and GF higher than 100 (or even higher than 1000) in full working strain range were reported following the crack-propagation mechanism. However, the intrinsic lack of flexibility in the brittle thin film/network greatly restricted this type of strain sensors to a limited working strain range, normally narrower than 20%, thus significantly

impeding their detection on human motion with large deformation of ≈50%. To improve the working strain range, turning the brittle device into flexible or stretchable device by embedding the conductive thin film/network into elastomer matrix was the most-widely used strategy.[19–24] In this case, the movement of polymer molecular chains would intend to accommodate the applied stress when stretching. Instead of crack formation, connected or overlapped materials in the conductive thin film or network would slide to reduce their overlapped area when stretching and thus decrease the electrical connection, resulting in the increase of electrical resistance.[6] Various stretchable strain sensors fabricated by integrating carbon and metal-based nanomaterials with elastomer matrix were reported to work well over 50% strain. Nevertheless, strain sensors based on this slippage (or disconnection) mechanism always suffered from nonlinearity response curve and limited GF, usually lower than 100, which restrained their monitoring on weak and subtle human motion. Generally, high sensitivity demands sensing material that can realize substantial structural changes even under tiny strain (crack-propagation mechanism dominated), while large stretchability requires structural connection or morphological integrity for sensing materials upon large deformation (slippage mechanism dominated).[8] However, it is still hard to integrate these two contradictory features into one sensing thin film.

To overcome this issue, efforts have been devoted to design sensing material with hierarchical structure to combine the slippage and crack-propagation mechanism into one strain sensor device.[8–10,25–27] Liu et al. introduced a strategy of thickness-gradient sensing films to fabricate strain sensor with gauge factor up to 161 and stretchability up to 150%.[8] Howbeit, the working strain with gauge factor higher than 100 was only limited in a small range of 0–2% where crack-propagation mechanism still dominated. Moreover, Liu et al. reported a strategy to combine the slippage mechanism and crack-propagation mechanism via designing a strain sensor with a fish-scale-like graphene-sensing layer. The strain sensor performed sensing behavior through the change of overlapping area of adjacent graphene-based slices caused by layer slippage in strain range of 0–60% and through crack formation induced by the layer separation in the strain range of 60–82%. Although a high gauge factor of 150 was achieved in the strain range of 60–82% thanks to the crack-propagation mechanism, the strain sensor still exhibited a low gauge factor of 16.2 under 0–60% due to the dominated slippage mechanism in this strain range. Thus, despite these advances in improving the sensing performance, the nonhomogeneous or nonuniform structure for these sensing materials could result in a nonlinear sensing manner divided into different sensing regions, each of which was dominated by either one of the two (crack-propagation and slippage) sensing mechanism. Thus, achievement of strain sensor with both large stretchability (working strain >50%) and high sensitivity (gauge factor >100 in full working strain range), coupled with linearity, low hysteresis and long-term durability, is still a grand challenge.[10,25] In addition, the fabrication method of many reported strain sensors relied on costly, complex and time-consuming microfabrication or deposition techniques, which inevitably hamper their low-cost integration, mass production, and commercialization.[13]

Recently, a homogeneous rigid network structure based on 2D MXene and 1D carbon nanotubes was fabricated into versatile strain sensors that can perform crack-propagation and slippage mechanism simultaneously when stretching.[26] Carbon nanotubes were able to bridge the microcracks induced by the rigid MXene-based network during stretching, leading to a great enhancement on the stretchability (up to ≈80%) for the brittle sensor while maintaining high sensitivity. Although a gauge factor lower than 100 was still obtained in large working strain range of 0–40%, this work inspires us that uniform composite network structure with rational design provides a good chance to take the merits of crack-propagation and slippage mechanism simultaneously to boost the sensing performance. In this work, we report on the development of a 0D–1D–2D ternary nanocomposite–based strain sensor that simultaneously exhibits high sensitivity (gauge factor >400) and large stretchability (working strain range >50%) through one-step screen-printing process with printing resolution up to 35 µm. The resistance changing behavior of the strain sensor shows low hysteresis and features four linear regions with linearity (R-square) all higher than 0.98. The gauge factor is up to 25, 466.2, 1000.2, and 2392.2 in four strain regions of 0–3%, 3–35%, 35–52%, and 52–62%, respectively. In addition, the strain sensor can withstand long-term strain cycles (up to 3000 cycles between 0% and 40% strain) and various stretching frequency. This high comprehensive sensing performance is enabled by the integration of layer-slippage and crack-propagation mechanism resulted from the synergistic effect of three nanocomponents within the sensing film: 1) 1D silver nanowire (AgNW) constructing highly electrical conductive network, 2) 2D graphene oxide (GO) facilitating the assemble of brittle but slidable layered structure, and 3) 0D fullerene (C60) working as lubricant agent to reduce the friction force between adjacent layered materials. When stretching, the brittle nature of the 0D–1D–2D ternary nanocomposite sensing film causes the formation and propagation of cracks but in a relative mild ratio since the layer slippage between adjacent layers caused by C60 can accommodate partial applied stress, thus boosting the stretchability while maintaining high sensitivity in broad working strain range. Additionally, the sensing performance is easily tuned through controlling the sensor structure by simply adjusting the printing parameters. The feasibility of this high-performance strain sensor is demonstrated by a series of human-motion–related detections with large and subtle strains.

2. Results and Discussion

The 0D–1D–2D ternary nanocomposite–based strain sensor was assembled via direct screen-printing from a GO–AgNW–C60 ternary aqueous ink on stretchable substrate (**Figure 1**a), and the ternary aqueous ink was prepared according to our previous published work (detailed in Experimental Section).[28] In brief, a diluted aqueous mixture of AgNW, GO, and C60 was prepared via mild sonication, followed by vacuum filtration to obtain a AgNW–GO–C60 hydrogel film. The collected AgNW–GO–C60 hydrogel film from the membrane filter was redispersed in a certain amount of distilled water with Fluorosurfactant FS-30 through strong agitation using VORTEX mixer to obtain the
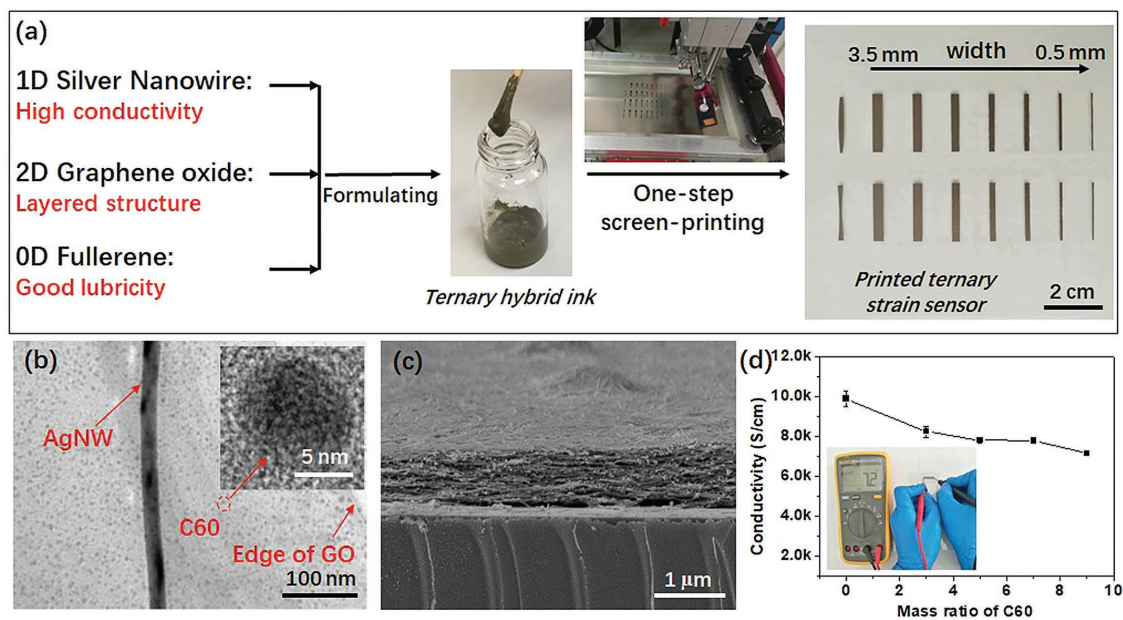
**ADVANCED
SCIENCE NEWS**
www.advancedsciencenews.com

**ADVANCED
FUNCTIONAL
MATERIALS**
www.afm-journal.de

Figure 1. a) Schematic of the screen-printing process for fabricating 0D–1D–2D ternary nanocomposite–based strain sensors. b) TEM image for the aqueous ink of GO–AgNW–C60$_{(7)}$. c) SEM image for the cross-section of GO–AgNW–C60$_{(7)}$ sensing film. d) Electrical conductivity of the ternary nanocomposite–based strain sensor with various mass ratio of C60. Inset image shows that the measured resistance for a GO–AgNW–C60$_{(7)}$ sensing film is 7.2 ohm.

final homogeneous printable gel-like GO–AgNW–C60 aqueous ink. C60, a molecule of carbon in the form of a 0D spherical hollow sphere, has been intensively investigated as solid lubricant due to its unique crystal structure and bonding.[29,30] The sensing performance of the 0D–1D–2D ternary nanocomposite–based film for the strain sensor was investigated by introducing different contents of C60 into the GO–AgNW system with fixed weight ratio of GO:AgNW at 15:85. Various strain sensors based on different nanocomposite films designated as GO–AgNW–C60$_{(0)}$, GO–AgNW–C60$_{(3)}$, GO–AgNW–C60$_{(5)}$, GO–AgNW–C60$_{(7)}$, and GO–AgNW–C60$_{(9)}$ were fabricated. The subscript number in brackets represents the mass ratio of C60 to total mass of GO and AgNW in the nanocomposite films. For instance, "(0)" indicates pure GO–AgNW film without adding of C60; "(3)" means that the mass ratio of C60 to GO and AgNW is 3:100. Moreover, a tiny amount of Fluorosurfactant FS-30, a nonionic polymeric fluorochemical surfactant, was added into GO–AgNW–C60 aqueous ink to promote the wettability and adhesive force between the nanocomposite film and stretchable polyurethane substrate. As can be seen in Figure 1a, strain sensors with diverse geometries (length of 2 cm and width decrease from 3.5 to 0.5 mm in step of 0.5 mm) can be fabricated by direct screen-printing the GO–AgNW–C60 aqueous inks on stretchable and hydrophilic polyurethane substrate (Figure S1 in the Supporting Information) via designed opening patterns on the screen stencil. Printing resolution up to 35 μm can be achieved by carefully controlling the printing parameter and rheological behavior for the GO–AgNW–C60 aqueous inks (Figure S2, Supporting Information), which make the integration of sensing array in micrometer scale for accurate measurement possible. The hydrophilic feature of the surface of polyurethane, which is treated by O$_2$ plasma, can guarantee the relative good adhesion force between GO in the

sensing film and stretchable substrate via H-bonding. In addition, the thickness of the ternary nanocomposite sensing film is facilely controlled by changing the solid concentration in the aqueous ink (Figure S3, Supporting Information). This strategy of fabricating strain sensor with controllable structure utilizing simple scalable one-step screen-printing process has great potential for scalable practical production.

Figure 1b and Figure S4 (Supporting Information) show the typical transmission electron microscope (TEM) image for aqueous ink of pure C60, GO–AgNW, and GO–AgNW–C60$_{(7)}$, and it is clearly seen that the C60 nanoparticles with multilayered structure and diameter of about 10 nm (Figure 1b) was present and uniformly distributed within the nanocomposite without aggregation. Cross-sectional scanning electron microscopy (SEM) image in Figure 1c displays that the internal layered structure of the nanocomposite sensing film, which is attributed to the existence of 2D GO nanosheets in the nanocomposite film.[31,32] It is noteworthy that no layered structure was observed for the pure AgNW films without GO (Figure S5, Supporting Information). This lamellar structure is a key structural factor to introduce slippage mechanism into the strain sensor during stretching. Moreover, the electrical conductivity of the GO–AgNW–C60 nanocomposite films were also evaluated as illustrated in Figure 1d. The conductivity of GO–AgNW–C60$_{(0)}$ achieved as high as ≈10 000 S cm^{-1} thanks to the highly conductive network assembled from AgNWs. Although conductivity declined with increase of C60 content in the nanocomposite film, all strain sensors exhibited electrical conductivity higher than 7000 S cm^{-1}, which is essential for sensing applications requiring low power consumption.[23,33]

The sensing performance of the 0D–1D–2D ternary nanocomposite–based strain sensors was evaluated by measuring the change of their relative resistance (($R − R_0$)/R_0, where
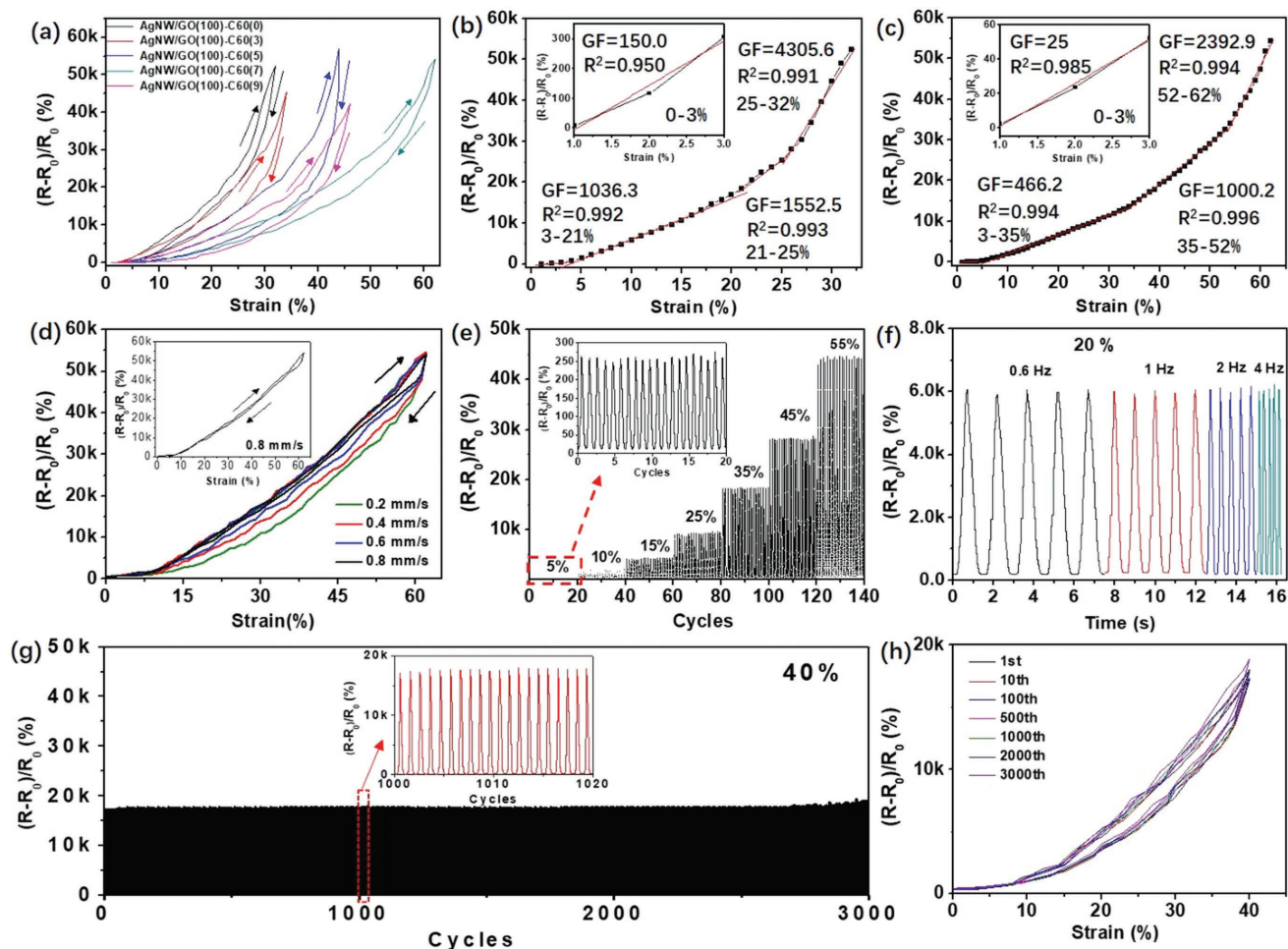
Figure 2. a) Typical relative resistance change-applied strain curves under one stretch/release cycle for GO–AgNW–C60$_{(0)}$, GO–AgNW–C60$_{(3)}$, GO–AgNW–C60$_{(5)}$, GO–AgNW–C60$_{(7)}$, and GO–AgNW–C60$_{(9)}$ strain sensors. The GF and linear behavior of b) GO–AgNW–C60$_{(0)}$ strain sensor and c) GO–AgNW–C60$_{(7)}$ strain sensor. d) Typical relative resistance change-applied strain curves under one stretch/release cycle for GO–AgNW–C60$_{(7)}$ strain sensor at various strain rates. e) Relative resistance change under various cyclic strains at a frequency of 1 Hz for the GO–AgNW–C60$_{(7)}$ strain sensor. f) Relative resistance variation of the GO–AgNW–C60$_{(7)}$ strain sensor at different frequency under 20% strain. g) Relative resistance change of GO–AgNW–C60$_{(7)}$ strain sensor during 3000 cycle of stretching and releasing between 0% and 40% strain at strain rate of 0.2 mm s^{-1}. Inset figure showing the detailed relative resistance change curves recorded between 1000 and 1020 stretch/release cycles. h) Typical relative resistance change-applied strain curves under specific stretch/release cycle of stretching and releasing between 0% and 40% strain for the GO–AgNW–C60$_{(7)}$ strain sensor.

R_0 and R are the resistance of strain sensor before stretching and under strain) under specific applied strain. All strain sensors were mounted on a motorized linear stage, and the resistance change was monitored in sync with deformation. Unless otherwise stated, all strain sensors were made with sensing film dimension of 3.5 mm in width, 2 cm in length, and about 0.9 μm in thickness and were stretched along the length direction. We first investigated the effect of C60 on the stretchability of the strain sensor. As shown in **Figure 2**a, the relative resistance changes increase with applied strain (ε). GO–AgNW–C60$_{(0)}$ sensor without addition of C60 can only be stretched to strain of 31% before turning into insulating. A clear phenomenon is observed: addition of C60 can enlarge the working strain range. While the mass ratio of C60 increase to "7," the working strain range of GO–AgNW–C60$_{(7)}$ strain sensor improve twice that of GO–AgNW–C60$_{(0)}$ strain sensor, to 62%. All strain sensors were stretched at strain rate of 0.2 mm s^{-1}.

Figure 2b,c and **Table 1** further studied the sensitivity of GO–AgNW–C60$_{(0)}$ and GO–AgNW–C60$_{(7)}$ strain sensor. It can be seen from Figure 2c that the sensing curve of the GO–AgNW–C60$_{(0)}$ strain sensor featured four linear regions: 0–3% with linearity of 0.950, 3–21% with linearity of 0.992, 21–25% with linearity of 0.993, and 25–31% with linearity of 0.991. The GF was calculated to be 150.0, 1036.3, 1552.5, and 4305.6 in these four linear regions respectively. This means that the GF achieves higher than 100 in the whole working strain range of 31% for the GO–AgNW–C60$_{(0)}$ strain sensor without C60. This high sensitivity coupled with good linearity is mainly attributed to the microcrack-propagation mechanism in the brittle binary nanocomposite sensing film. Stretching resulted in producing and enlargement of microcracks in the GO–AgNW–C60$_{(0)}$ thin film, which significantly restricted the electrical conduction pathway based on AgNW networks through the sensing films (as discussed in details below).[6] As to the GO–AgNW–C60$_{(7)}$ strain

**ADVANCED
SCIENCE NEWS**
www.advancedsciencenews.com

**ADVANCED
FUNCTIONAL
MATERIALS**
www.afm-journal.de

Table 1. Comparison of working strain range, GF and linearity for GO–AgNW–C60$_{(0)}$ and GO–AgNW–C60$_{(7)}$ strain sensors.

Strain sensor	GO–AgNW–C60(0)				GO–AgNW–C60(7)			
Strain range	0–3%	3–21%	21–25%	25–32%	0–3%	3–35%	35–52%	52–62%
GF	150.0	1036.3	1552.5	4305.6	25	466.2	1000.2	2392.9
Linearity	0.95	0.992	0.993	0.991	0.985	0.994	0.996	0.994

sensor, although working strain range increased by 100% compared to that of the GO–AgNW–C60$_{(0)}$ strain sensor, four similar linear regions with linearity all >0.98 are still observed: 0–3% with linearity of 0.985, 3–35% with linearity of 0.994, 35–52% with linearity of 0.996, and 52–62% with linearity of 0.994. Importantly, the GF was measured to as high as be 25.0, 466.2, 1000.2, and 2392.9 in four corresponding linear regions, respectively. This suggests that the GO–AgNW–C60$_{(7)}$ strain sensor exhibits GF larger than 400 in a broad working strain range from 3% to 62%, reaching the challenge requirement of high sensitivity (gauge factor >100) and large stretchability (working strain >50%) simultaneously. Normally, strain sensors with large GF typically responded to the applied strain with high nonlinearity and small working strain range, and vice versa.[6] As can be seen from the comparison in **Figure 3**, GO–AgNW–C60$_{(7)}$ strain sensor possesses the best GF (2392.9) among all the previously reported strain sensors in challenge region of sensing performance achieving working strain >50% and gauge factor >100 at the same time.[8–12,14,16,17,21–26,34] Although the GF for GO–AgNW–C60$_{(7)}$ strain sensor in strain of 0–3% was lower than 100, the value of 25 is still predominant among these recently reported results in the same working strain range.[19,21–24,35,36]

The linearity response for the nanocomposite sensing film should be the result from the homogeneous crack formation over the whole sensing film (**Figure 4**), which is frequently observed for brittle strain sensor having uniform structure and limited stretchability.[11,18] However, it is interesting to see that the cracks exhibit different structure or morphology under different strain ranges (Figure 4). For example, parallel linear microcracks are formed on the GO–AgNW–C60$_{(7)}$

sensing film when 10% and 20% strain are applied on the strain sensor, whereas vertical linear microcracks appear to bridge the parallel linear microcracks when applied strain is increased to 40%; while the applied strain is enhanced to 60%, most linear cracks turn into wavy structure. This phenomenon of cracks propagating into different structures under different strain range could be the important reason that cause the sensing curves divided into different linear regions.[6]

Moreover, it can be clearly seen from Figure 2d and Figure S6 (Supporting Information) that the hysteresis behavior for sensing response curves from GO–AgNW–C60$_{(7)}$ strain sensor is heavily dependent on the strain rate, and faster strain rate results in smaller hysteresis. When the strain rate is increased to 0.8 mm s^{-1}, the curves for the typical relative resistance change under applied stretching strain and releasing strain are almost overlapping (inset in Figure 2d), indicative of negligible hysteresis. Such low hysteresis is attributed to the fact that no viscoelastic polymer additives or matrix is introduced into this ternary nanocomposite–based sensing film.[6]

In addition to high sensitivity, broad working strain range and low hysteresis, the 0D–1D–2D ternary nanocomposite–based strain sensor also exhibits excellent stability and reliability in the sensing performance. Figure 2e displays the relative resistance change of the GO–AgNW–C60$_{(7)}$ strain sensor under various cyclic strains at a frequency of 1 Hz (strain rate of 0.2 mm s^{-1}). At the maximum strains of 5%, 10%, 15%, 25%, 35%, 45%, and 55%, the variations in the relative resistance were measured to be approximate 2.64, 19.10, 42.57, 90.46, 183.12, 280.15, and 444.86, respectively. These values are coincident with the results shown in Figure 2a,c. In contrast, the GO–AgNW–C60$_{(0)}$ strain sensor without addition of C60 can only present reliable cyclic sensing performance below 30% strain due to the stretchability limitation (Figure S7, Supporting Information). Figure 2f further illustrates the relative resistance variation of the GO–AgNW–C60$_{(7)}$ strain sensor at various frequency under 20% strain, and no frequency dependence for the electrical response is observed. The relative resistance changes at a maximum strain of 20% were almost constant at stretching frequency ranging from 0.6 to 4 Hz. Figure 2g depicts the relative resistance change of the GO–AgNW–C60$_{(7)}$ strain sensor during 3000 cycles of stretching and releasing between 0% and 40% strain at strain rate of 0.2 mm s^{-1}. Both the peak and baseline resistance changes remain stable during the first 2600 cycles (as further confirmed in the inset figure in Figure 2g). Then, the peak resistance changes creep gradually as the cyclic number increases. This indicates the fully reversible structural change for the strain sensor during the 2600 cycles of stretching/releasing test under 40% strain. When the applied strain is increased to 50% (Figure S8, Supporting Information), the baseline resistance changes maintain fairly
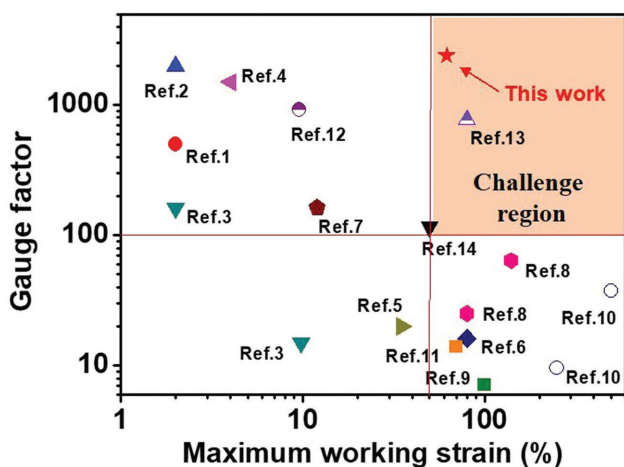

Figure 3. Comparison of the GF and maximum working strain range of the present GO–AgNW–C60$_{(7)}$ strain sensor with various recent published results.
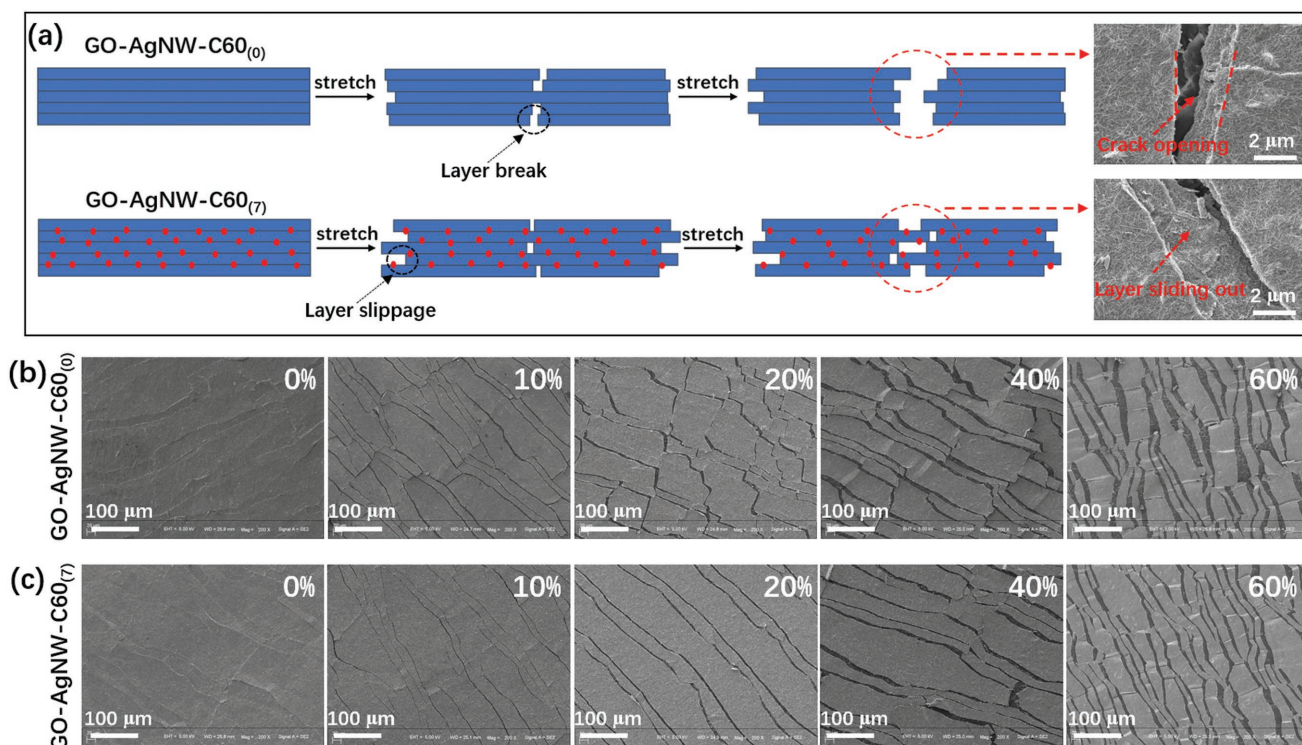
Figure 4. a) Schematic illustration of sensing mechanism for GO–AgNW–C60$_{(0)}$ and GO–AgNW–C60$_{(7)}$ sensing films under stretching. Inset upper surface SEM shows the gap between crack edges in GO–AgNW–C60$_{(0)}$ sensing film. Inset lower SEM shows layers partially sliding out inside the crack in GO–AgNW–C60$_{(7)}$ sensing film. Surface SEM images for b) the GO–AgNW–C60$_{(0)}$ and c) the GO–AgNW–C60$_{(7)}$ sensing films at various applied strains.

stable during the whole cyclic test; in the meanwhile, the peak resistance changes perform relative smooth at the first 500 cycles, but then rise slowly with cycling. This relative low durability for the GO–AgNW–C60$_{(7)}$ strain sensor under 50% is mainly caused by the limited adhesive force between the sensing film and polyurethane substrate. A small degree of sensing film detaching from the substrate is observed under large strain (Figure 4). Moreover, typical relative resistance changes for the GO–AgNW–C60$_{(7)}$ strain sensor under different specific stretch/release cycles between 0% and 40% strain are also detailed in Figure 2h. All the sensing curves at 1st, 10th, 100th, 500th, 1000th and 2000th stretch/release cycles overlap well, indicative of good monotonicity of the sensor.

Next, we further investigated the sensing mechanism for the 0D–1D–2D ternary nanocomposite–based sensing film. Considering the intrinsic layered structure of the nanocomposite film, there mainly existing two types of motion models inside the sensing films during stretching: fracture of the lamellar structures, which corresponds to crack-propagation sensing mechanism, and slippage of adjacent layers, which corresponds to slippage sensing mechanism, as illustrated in simplified mechanism modes in Figure 4a. To understand the effect of C60 on the sensing mechanism for the ternary strain sensor, both the GO–AgNW–C60$_{(0)}$ and GO–AgNW–C60$_{(7)}$ sensing films were stretched under the same specific strain and characterized by surface SEM. As shown in Figure 4b,c, microcracks form and propagate homogeneously as the applied strain increases in both films. This suggests that the relative resistance changes

for the sensing films with or without C60 were all mainly controlled by the crack-propagation mechanism, which thus can guarantee the high sensitivity and linearity for both sensing devices as discussed in Figure 2 above. However, it is clearly seen in Figure 4b,c that crack density and crack size in GO–AgNW–C60$_{(0)}$ and GO–AgNW–C60$_{(7)}$ sensing films are different. Figure S9 (Supporting Information) compares the crack density (Figure S9a, Supporting Information) and average crack opening between two crack edges (Figure S9b, Supporting Information) in the GO–AgNW–C60$_{(0)}$ and GO–AgNW–C60$_{(7)}$ sensing films under different applied strains. The data were summarized from their SEM images. Compared to the GO–AgNW–C60$_{(0)}$, GO–AgNW–C60$_{(7)}$ sensing film exhibits lower crack density and smaller crack opening size under all strains. This indicates that the existence of C60 can suppress the crack formation and growth in the 0D–1D–2D ternary nanocomposite sensing films to a certain extent. According to the Johnson, Kendall, and Roberts theory, the adhesive force between two material surfaces can be calculated from Equation (1)[37]

$$F_a = (3\pi R W_{AB} e^{-\sigma/\sigma_0}) / 2 \tag{1}$$

where R is the radius of the testing probe, σ is the roughness of the probe, σ_0 is the constant, and W_{AB} is the dispersive work of adhesion per unit area of surface for material A in contact with surface for material B, which can be expressed by Equation (2)[37]

$$W_{AB} = 2(\gamma_A \gamma_B)^{1/2} \tag{2}$$

**ADVANCED
SCIENCE NEWS**
www.advancedsciencenews.com

**ADVANCED
FUNCTIONAL
MATERIALS**
www.afm-journal.de

where γ_A and γ_B are the surface energies of for material A and B, respectively. In the case of our nanocomposite sensing films, the surface energies of GO and C60 have been measured to be 62.1 and 40.64 mJ m^{-2} at ambient conditions, respectively, according to previously published literatures.[29,38] Hence, the interfacial energy between GO and GO can be calculated to be $W_{GO-GO} = 100.47$ mJ m^{-2}, and the interfacial energy between GO and C60 was calculated to be $W_{C60-C60} = 81.28$ mJ m^{-2}. This indicates that the introduction of C60 can decrease the friction force between GO-based layers and thus facilitates the sliding between adjacent layers. Therefore, when strain was applied on the GO–AgNW–C60(7) sensing film, the slippage between adjacent layers inside the 0D–1D–2D nanocomposite film could accommodate partial stress applied on the sensing film, compress the crack propagation in a certain degree, and expand the working strain range for the strain sensor. As confirmed by inset SEM images in Figure 3a, compared to the GO–AgNW–C60(0) sensing film without C60, GO–AgNW–C60(7) sensing film exhibits much greater degree of layer sliding inside the crack under the same strain. Moreover, the synergistic effect of AgNW, GO, and C60 in the sensing film is further evaluated by typical tensile stress–strain curves of freestanding nanocomposites films as shown in Figure S10 (Supporting Information). GO–AgNW–C60(0) and GO–AgNW–C60(7) nanocomposite films are provided with high Young's modulus of 13.77 and 11.52 GPa, respectively. This high stiffness for both sensing films should be attributed to the nacre-based structure of GO and AgNW-based nanocomposite.[31,32,39,40] Importantly, addition of C60 decrease the Young's modulus by only ≈16% but greatly increase the break of elongation by almost 100%, consistent with the enhancement for the working strain range (Figure 2a). This further confirms that the existence of GO and AgNW can guarantee the stiffness of the sensing film and provide high

sensitivity through crack-propagation mechanism, and the addition of lubricant C60 can render high working strain via layer-slippage mechanism.

It is known that the sensing performance of strain sensors is closely related to their geometries.[13,34] However, barely works have systematically investigated the device structure effect probably due to the complicated or uncontrollable device fabrication process.[13,34] In contrast, the 0D–1D–2D ternary nanocomposite–based strain sensor can be fabricated through simple one-step screen-printing process. To systematically evaluate the effects of the device geometries on the sensing performance of strain sensor, various GO–AgNW–C60(7) strain sensors with diverse shape or structure were fabricated by via facilely tuning the printing parameter and ink concentration as detailed in Experimental Section. First, to reveal the effect of device width on the sensing performance, rectangle GO–AgNW–C60(7) sensing films with fixed length (2 cm) and thickness (1.3 μm) but different width (1.5, 2.5, and 3.5 mm) were fabricated, and the corresponding devices were denoted as GO–AgNW–C60(7)–W1.5, GO–AgNW–C60(7)–W2.5, and GO–AgNW–C60(7)–W3.5 (Figure 1a), respectively. **Figure 5**a compared their relative resistance change as a function of working strain. A clear trend shows that increase in device width results in enhancement on both sensitivity and stretchability for GO–AgNW–C60(7) strain sensors. As the device width increase from 1.5 to 3.5 mm, the maximum GF increase from 1459.0 to 1982.9, and the working strain improved greatly from 18% to 55%, enhanced by ≈200%. While the strain sensors are stretched along the device length direction, the crack in the sensing film will form and propagate along the width direction. Sensing films with larger width can alleviate the applied strain more effectively due to the increase of device cross-section area. Thus, the effect of layer-slippage mechanism will play a more important role in the
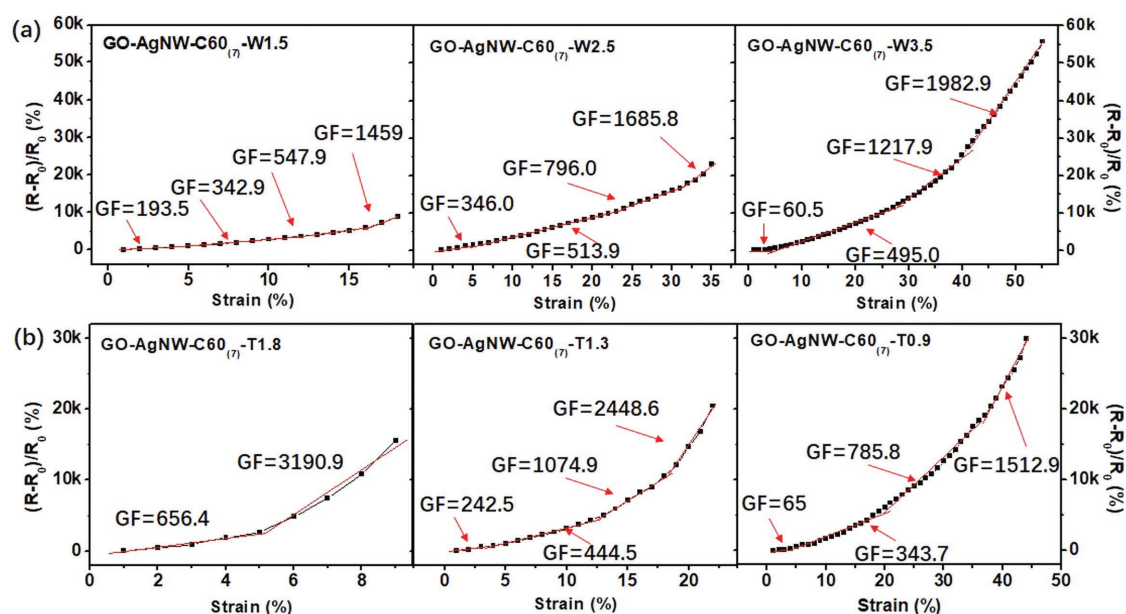

Figure 5. a) Relative change in resistance as a function of applied strain for GO–AgNW–C60(7)–W1.5, GO–AgNW–C60(7)–W2.5, and GO–AgNW–C60(7)–W3.5 strain sensors with fixed device length (2 cm) and thickness (1.3 μm) but different width (1.5, 2.5, and 3.5 mm). b) Relative change in resistance versus applied strain for GO–AgNW–C60(7)–T0.9, GO–AgNW–C60(7)–T1.3, and GO–AgNW–C60(7)–T1.8 strain sensors with fixed device length (2 cm) and width (2 mm) but different thickness (0.9, 1.3, and 1.8 μm).
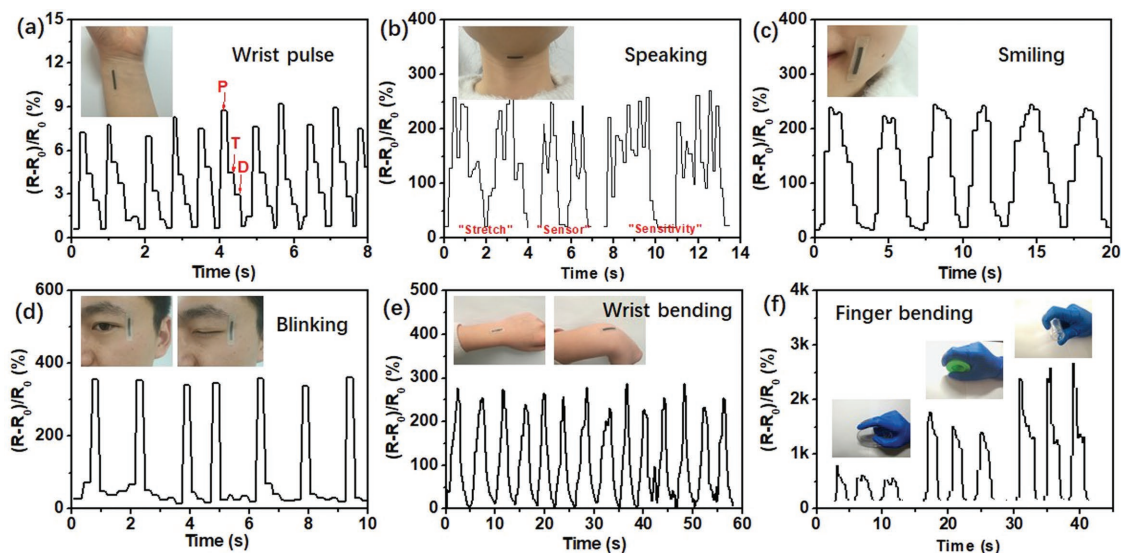
**ADVANCED
SCIENCE NEWS**
www.advancedsciencenews.com

**ADVANCED
FUNCTIONAL
MATERIALS**
www.afm-journal.de

Figure 6. Monitoring of human motion using GO–AgNW–C60$_{(7)}$ strain sensor. Relative resistance change of a) wrist pulse, b) speaking "stretch," "sensor," and "stretchability," respectively, c) facial expression, d) blinking, e) wrist bending, and f) finger bending to different degree.

sensing process as the device width become larger. Moreover, the enlargement of microcracks along the width direction in the sensing film would perform longer distance to separate the film completely as the width become larger. Both effects will lead to the increase of the working strain in the ternary strain sensors with larger device width. Then, to study the effect of device thickness on the sensing performance, GO–AgNW–C60$_{(7)}$ strain sensors with fixed length (2 cm) and width (2 mm) but different thickness (0.9, 1.3, and 1.8 µm) are made, and the corresponding devices were denoted as GO–AgNW–C60$_{(7)}$–T0.9, GO–AgNW–C60$_{(7)}$–T1.3, and GO–AgNW–C60$_{(7)}$–T1.8 (Figure S3, Supporting Information), respectively. Figure 5b plots the relative change in resistance of the strain sensor with various thicknesses as a function of applied strain. Obviously, the stretchability of the strain sensor increases with the device thickness decreases. The highest GF for the rigid GO–AgNW–C60$_{(7)}$–T1.8 strain sensor with device thickness of 1.8 µm was calculated to be 3130.9 in small working strain range of 5–9%. Although the maximum GF drops to 1512.9 as the device thickness declines to 0.9 from 1.8 µm, the working strain range shows a significant increase from 9% to 44%. This stretchability increase can be attributed to the fact that reducing thickness in the film can render the brittle thin film flexible.[18] Thus, the sensing performance of the 0D–1D–2D ternary nanocomposite–based strain sensor can be predicted and controlled by carefully designing the device structure through facilely adjusting the printing parameter.

The excellent comprehensive performance, including high sensitivity, broad working strain range and superior stability and reliability, enables the 0D–1D–2D ternary nanocomposite–based strain sensor detect full-spectrum human motion. Based on its ability to sense low strain (<3%) with high GF, GO–AgNW–C60$_{(7)}$ strain sensor can monitor subtle strain of human body activities such as pulse, facial expression, and phonation. As shown in **Figure 6**a, the strain sensor was mounted on a wrist to detect the human pulse waveforms. Distinct radial pulse wave including diastolic (D) wave, tidal (T) wave, and

percussion (P) wave, were clearly and promptly recorded,[23,24] indicating the high sensitivity of the GO–AgNW–C60$_{(7)}$ strain sensor at subtle strain. The strain sensor can also be fixed onto the throat to detect the small epidermis and muscle deformation during speaking to distinguish phonation. Clear, characteristic and repeatable signal patterns were displayed in Figure 6b when wearer spoke different polysyllabic words, such as "stretch," "sensor," and "stretchability." Moreover, the ternary strain sensor is able to measure tiny muscle movement induced by facial expression by attaching on human face. The repeatable signals of relative resistance change corresponding to facial expression of changing from poker face to smile face (Figure 6c) and blinking (Figure 6d) were precisely recorded. On the other hand, human joint motion usually requires stretching epidermis to large strain up to 50% or even higher. Thus, the GO–AgNW–C60$_{(7)}$ strain sensor can also be applied to detect large human body movement such as human joint motion thanks to its high GF (>400) in large working strain range of 3–62%. As shown in Figure 6e,f, strain sensors were attached on wrist and finger joints respectively to monitor their bending and relaxing motions. Different bending degrees can be precisely and rapidly tracked by monitoring the relative change of the resistance.

3. Conclusion

In summary, 0D–1D–2D ternary nanocomposite–based strain sensor with combination performance of outstanding sensitivity, broad working strain range, linear response behavior, low hysteresis, and long-term stability and reliability has been developed via a simple fabrication strategy of one-step screen-printing functional aqueous ink composed of 1D AgNW, 2D GO, and 0D C60. The effect of C60 and device geometries on the sensing performance was systematically investigated. The sensing performance is easily to be designed and predicted through controlling the sensor structure by simply adjusting

the printing and ink parameters. The C60 work as lubricant agent to lower the internal friction force and introduce layer-spillage during crack propagation in the ternary strain sensor under applied strain, thus boosting the stretchability (>50% strain) while maintaining superior sensitivity (>400 in working strain range > 50%). These excellent features coupled with facile device fabrication method enable the printed 0D–1D–2D ternary nanocomposite–based strain sensor precisely detect full-spectrum human motion ranging from pulse with tiny strain to joint motion with large strain.

4. Experimental Section

Raw Materials: AgNWs were synthesized with average diameter and length ≈40 nm and ≈20 μm, respectively.[41] GO was prepared from graphite following the modified Hummers method.[42] The average lateral size was 5–10 μm and thickness was 0.8 nm. Water-soluble C60 was purchased from Nanjing XFNANO Materials Tech Co., Ltd. Fluorosurfactant FS-30 was purchased from 3M. Polyurethane (4055IC) was obtained from Yantai Wanhua Polyurethane Co., Ltd.

Preparation of GO–AgNW–C60 Aqueous Ink: The ternary ink was prepared according to our previously published work.[28] First, 2 mg mL^{-1} GO dispersion was prepared by dispersing GO in distilled water via sonication for 2 h, followed by adjusting the pH value to 6.5 through adding moderate 0.2 M NaOH aqueous solution. Subsequently, 10 mg mL^{-1} C60 aqueous solution was prepared by dispersing C60 to distilled water via stirring for 2 h, followed by mixing with GO solution for 24 h to make GO–C60 solution. GO–C60 solution was then added into the 1 mg mL^{-1} AgNWs aqueous solution with AgNWs to GO weight ratio of 85:15. After sonication for about 10 min, the ternary mixture of AgNW, GO, and C60 was vacuum filtration using PTFE membrane filter with pore size of 0.45 μm, followed by washing with 50 mL distilled water for five times, to make AgNW–GO–C60 ternary film. The collected AgNW–GO–C60 film from the membrane filter was redispersed in a certain amount of distilled water with Fluorosurfactant FS-30 through strong agitation using VORTEX mixer at 1000 rpm for 2 h to obtain the final homogeneous printable GO–AgNW–C60 aqueous ink. Four GO–AgNW–C60 ink with fixed GO and AgNW mass ratio but different C60 contents were made, including GO:AgNW:C60 = 85:15:3, 85:15:5, 85:15:7, and 85:15:9, respectively. Pure GO and AgNW mixture solution, without addition of C60, was also made at the mass ratio of 85:15 for comparison purpose.

Fabrication of 0D–1D–2D Ternary Nanocomposite–Based Strain Sensor: Screen-printing process was performed on a TC-4060k screen printer (Dongguan Ta Chen Screen Printing Machine&Materials Co., Ltd), and a precision stainless steel thin-film–based screen stencil (thickness of 80 μm) with designed openings was used. The screen-printing parameters including the angles between squeegee and stencil, printing speed, printing force, and distance between stencil and substrates were tuned and optimized. After printing, the sensor patterns were dried at ambient conditions for 3–5 min to evaporate the water before all tests. Various strain sensors based on different nanocomposite films designated as GO–AgNW–C60$_{(0)}$, GO–AgNW–C60$_{(3)}$, GO–AgNW–C60$_{(5)}$, GO–AgNW–C60$_{(7)}$, and GO–AgNW–C60$_{(9)}$ were fabricated from the GO:AgNW:C60 aqueous inks with fixed GO and AgNW mass ratio but different C60 contents as mentioned above. The subscript number in brackets represents the mass ratio of C60 to total mass of GO and AgNW in the nanocomposite films. Moreover, various thickness for the ternary strain sensors can be obtained by fixing mass ratio of GO, AgNW and C60 but tuning the contents of water in the aqueous inks.

Characterization: The strain-resistance tests were carried on using a motorized linear stage with built-in controller (Zolix Inc.) with a Keithley 2000 digital multimeter used to monitor the resistance change. The SEM characterizations were carried out using field-emission scanning electron microscopy (JSM-7800) at an accelerating voltage of 5.0 kV.

To test the sensing films under stretched state, samples were first stretched to the specific strain and then stuck to sample stage using thermal-curable adhesives to firmly fix the deformation of the testing samples. TEM images were taken using a transmission electron microscope (JEM-2800, Japan). The electric conductivity was tested by digital and intelligent four-probe meter (ST2258C). The typical stress–strain curves were measured by Dynamic Mechanical Thermal Analyzer (DMA Q800). To make the testing sample, the GO–AgNW–C60$_{(0)}$ and GO–AgNW–C60$_{(7)}$ aqueous inks were poured into a rectangular sunken, followed by drying the inks at 60 °C for 2 h. Then, the nanocomposite films were peeled off and trimmed into testing samples with length of 30 mm, width of 3 mm, and thickness of 40 μm. The test length for all samples is 15 mm, and the test rate is 0.1 mm s^{-1}. The fitting area is 0–0.2% to calculate the Young's modulus.

Supporting Information

Supporting Information is available from the Wiley Online Library or from the author.

Conflict of Interest

The authors declare no conflict of interest.

[1] G. J. N. Wang, A. Gasperini, Z. Bao, *Adv. Electron. Mater.* **2018**, *4*, 1700429.

[2] W. Liu, M.-S. Song, B. Kong, Y. Cui, *Adv. Mater.* **2017**, *29*, 1603436.

[3] Z. Lou, L. Li, L. Wang, G. Shen, *Small* **2017**, *13*, 1701791.

[4] X. Wang, Z. Liu, T. Zhang, *Small* **2017**, *13*, 1602790.

[5] T. T. Tung, M. J. Nine, M. Krebsz, T. Pasinszki, C. J. Coghlan, D. N. H. Tran, D. Losic, *Adv. Funct. Mater.* **2017**, *27*, 1702891.

[6] M. Amjadi, K. U. Kyung, I. Park, M. Sitti, *Adv. Funct. Mater.* **2016**, *26*, 1678.

[7] S. Gong, D. T. H. Lai, B. Su, K. J. Si, Z. Ma, L. W. Yap, P. Guo, W. Cheng, *Adv. Electron. Mater.* **2015**, *1*, 1400063.

[8] Z. Liu, D. Qi, P. Guo, Y. Liu, B. Zhu, H. Yang, Y. Liu, B. Li, C. Zhang, J. Yu, B. Liedberg, X. Chen, *Adv. Mater.* **2015**, *27*, 6230.

[9] Q. Liu, J. Chen, Y. Li, G. Shi, *ACS Nano* **2016**, *10*, 7901.

[10] X. Xiao, L. Yuan, J. Zhong, T. Ding, Y. Liu, Z. Cai, Y. Rong, H. Han, J. Zhou, Z. L. Wang, *Adv. Mater.* **2011**, *23*, 5440.

[11] D. Kang, P. V. Pikhitsa, Y. W. Choi, C. Lee, S. S. Shin, L. Piao, B. Park, K. Y. Suh, T. Il Kim, M. Choi, *Nature* **2014**, *516*, 222.

[12] K. K. Kim, S. Hong, H. M. Cho, J. Lee, Y. D. Suh, J. Ham, S. H. Ko, *Nano Lett.* **2015**, *15*, 5240.

[13] S. Zhang, L. Cai, W. Li, J. Miao, T. Wang, J. Yeom, N. Sepúlveda, C. Wang, *Adv. Electron. Mater.* **2017**, *3*, 1700067.

[14] G. Shi, Z. Zhao, J. H. Pai, I. Lee, L. Zhang, C. Stevenson, K. Ishara, R. Zhang, H. Zhu, J. Ma, *Adv. Funct. Mater.* **2016**, *26*, 7614.

[15] X. Liao, Q. Liao, X. Yan, Q. Liang, H. Si, M. Li, H. Wu, S. Cao, Y. Zhang, *Adv. Funct. Mater.* **2015**, *25*, 2395.

[16] T. Yang, W. Wang, H. Zhang, X. Li, J. Shi, Y. He, Q. S. Zheng, Z. Li, H. Zhu, *ACS Nano* **2015**, *9*, 10867.

[17] X. Li, R. Zhang, W. Yu, K. Wang, J. Wei, D. Wu, A. Cao, Z. Li, Y. Cheng, Q. Zheng, R. S. Ruoff, H. Zhu, *Sci. Rep.* **2012**, *2*, 870.

[18] Y. W. Choi, D. Kang, P. V. Pikhitsa, T. Lee, S. M. Kim, G. Lee, D. Tahk, M. Choi, *Sci. Rep.* **2017**, *7*, 40116.

[19] C. S. Boland, U. Khan, G. Ryan, S. Barwich, R. Charifou, A. Harvey, C. Backes, Z. Li, M. S. Ferreira, M. E. Möbius, R. J. Young, J. N. Coleman, *Science* **2016**, *354*, 1257.

[20] C. S. Boland, U. Khan, C. Backes, A. O. Neill, J. Mccauley, S. Duane, R. Shanker, Y. Liu, I. Jurewicz, A. B. Dalton, J. N. Coleman, *ACS Nano* **2014**, *8*, 8819.

[21] C. Yan, J. Wang, W. Kang, M. Cui, X. Wang, C. Y. Foo, K. J. Chee, P. S. Lee, *Adv. Mater.* **2014**, *26*, 2022.

[22] M. Amjadi, A. Pichitpajongkit, S. Lee, S. Ryu, I. Park, *ACS Nano* **2014**, *8*, 5154.

[23] C. Wang, X. Li, E. Gao, M. Jian, K. Xia, Q. Wang, Z. Xu, T. Ren, Y. Zhang, *Adv. Mater.* **2016**, *28*, 6640.

[24] M. Zhang, C. Wang, H. Wang, M. Jian, X. Hao, Y. Zhang, *Adv. Funct. Mater.* **2017**, *27*, 1604795.

[25] J. Zhou, X. Xu, Y. Xin, G. Lubineau, *Adv. Funct. Mater.* **2018**, 1705591, https://doi.org/10.1002/adfm.201705591.

[26] Y. Cai, J. Shen, G. Ge, Y. Zhang, W. Jin, W. Huang, J. Shao, J. Yang, X. Dong, *ACS Nano* **2018**, *12*, 56.

[27] Y. Jiang, Z. Liu, N. Matsuhisa, D. Qi, W. R. Leow, H. Yang, J. Yu, G. Chen, Y. Liu, C. Wan, Z. Liu, X. Chen, *Adv. Mater.* **2018**, *30*, 1706589.

[28] S. Liu, J. Li, X. Shi, E. Gao, Z. Xu, H. Tang, K. Tong, Q. Pei, J. Liang, Y. Chen, *Adv. Electron. Mater.* **2017**, *3*, 1700098.

[29] X. Ma, B. Wigington, D. Bouchard, *Langmuir* **2010**, *26*, 12886.

[30] Y. Yao, X. Wang, J. Guo, X. Yang, B. Xu, *Mater. Lett.* **2008**, *62*, 2524.

[31] S. Wan, Q. Cheng, *Adv. Funct. Mater.* **2017**, *27*, 1703459.

[32] S. Wan, F. Xu, L. Jiang, Q. Cheng, *Adv. Funct. Mater.* **2017**, *27*, 1605636.

[33] J. Liang, L. Li, K. Tong, Z. Ren, W. Hu, X. Niu, Y. Chen, Q. Pei, *ACS Nano* **2014**, *8*, 1590.

[34] Y. Heo, Y. Hwang, H. S. Jung, S. H. Choa, H. C. Ko, *Small* **2017**, *13*, 1700070.

[35] C. Pang, G. Y. Lee, T. Il Kim, S. M. Kim, H. N. Kim, S. H. Ahn, K. Y. Suh, *Nat. Mater.* **2012**, *11*, 795.

[36] S. Zhao, L. Guo, J. Li, N. Li, G. Zhang, Y. Gao, J. Li, D. Cao, W. Wang, Y. Jin, R. Sun, C. P. Wong, *Small* **2017**, *13*, 1700944.

[37] J. Li, T. Gao, J. Luo, *Adv. Sci.* **2018**, *5*, 1870018.

[38] S. Wang, Y. Zhang, N. Abidi, L. Cabrales, *Langmuir* **2009**, *25*, 11078.

[39] H. L. Gao, Y. B. Zhu, L. B. Mao, F. C. Wang, X. S. Luo, Y. Y. Liu, Y. Lu, Z. Pan, J. Ge, W. Shen, Y. R. Zheng, L. Xu, L. J. Wang, W. H. Xu, H. A. Wu, S. H. Yu, *Nat. Commun.* **2016**, *7*, 12920.

[40] O. C. Compton, S. W. Cranford, K. W. Putz, Z. An, L. C. Brinson, M. J. Buehler, S. T. Nguyen, *ACS Nano* **2012**, *6*, 2008.

[41] B. Li, S. Ye, I. E. Stewart, S. Alvarez, B. J. Wiley, *Nano Lett.* **2015**, *15*, 6722.

[42] J. Liang, Y. Huang, L. Zhang, Y. Wang, Y. Ma, T. Cuo, Y. Chen, *Adv. Funct. Mater.* **2009**, *19*, 2297.